Element specific hysteresis of $La_{0.7}Sr_{0.3}MnO_3$—$SrRuO_3$ (LSMO-SRO) heterostructures

A. F. Schäffer,[1] L. Chotorlishvili,[1] I. V. Maznichenko,[1] A. Ernst,[2,3,4] K. Dörr,[1] I. Mertig,[1,2] and J. Berakdar[1]
[1]*Institut für Physik, Martin-Luther-Universität Halle-Wittenberg, 06099 Halle, Germany*
[2]*Max-Planck-Institut für Mikrostrukturphysik, Weinberg 2, D-06120 Halle, Germany*
[3]*Institute for Theoretical Physics, Johannes Kepler University, Altenberger Straße 69, 4040 Linz, Austria*
[4]*Donostia International Physics Center (DIPC), 20018 San Sebastián/Donostia, Basque Country, Spain*

(Received 19 April 2018; accepted 4 July 2018; published online 19 July 2018)

The ferromagnetic oxides $La_{0.7}Sr_{0.3}MnO_3$ (LSMO) and $SrRuO_3$ (SRO) couple antiferromagnetically, leading to a canted spin-structure at the interface's proximity. Performing first-principles calculations in combination with Monte Carlo and finite temperature micromagnetic simulations, we explore possible magnetic phases and find a distinctive element specific hysteresis behavior whose dependence on external parameters is analyzed. The results reveal the interplay of magnetic anisotropy and exchange coupling at the interface for the appearance of interfacial spin canting and unusual magnetic switching which are of strong relevance for spintronic devices. In particular, the different coercive fields for SRO and LSMO allow performing selective switching of SRO and LSMO layers. https://doi.org/10.1063/1.5036811

In antiferromagnetic/ferromagnetic multilayers, a ferromagnetic state can be pinned by the hard magnetic behavior of the adjacent antiferromagnetic layer. This phenomenon, in which the interfacial exchange interaction plays a key role, was first reported in 1957[1] and termed exchange bias (EB) or exchange anisotropy. Its manifestation resembles, however, the influence of a directional magnetic field rather than a uniaxial magnetic anisotropy. One observes, namely, a (thickness, temperature, and material-dependent) shift in the hysteresis loop with respect to variations in the magnetic field.[2] This shift is called exchange bias field. Generally, the shape of the hysteresis loop may also be modified or become asymmetric due to EB.[3] A number of important applications of EB rely on the EB-induced pinning of the magnetization of a soft ferromagnetic layer and the anisotropic magnetoresistance with respect to the magnetization direction.[4–10] Spin valve read heads and magnetic random access memory circuits[11] are examples, where EB is utilized.

EB was also found useful for magnetoelectric switching,[10] which hints at the potential of possible EB-type phenomena in magnetoelectric and oxide-based multilayers,[13–17] for both sizable EB and magnetoelectric coupling strengths are found at interfaces. The positive EB in epitaxial $La_{2/3}Sr_{1/3}MnO_3$ (LSMO)/$SrRuO_3$ (SRO) with antiferromagnetic interfacial coupling was discovered in Ref. 12. Due to the strong anisotropy in the SRO, this material mimics the AFM part, which is usually used in classical EB systems. In fact, an x-ray magnetic circular dichroism experiment, which provides an element specific magnetic characterization, revealed a remarkable correlation between the reversal of Mn and Ru magnetic moments at the MnO_2—SrO interface in $La_{0.7}Sr_{0.3}MnO_3$—$SrRuO_3$ (LSMO-SRO) heterostructures.[18] The coupling between the ferromagnetic LSMO layer and SRO is antiferromagnetic, pointing so to an exchange-bias-type effect at the MnO_2—SrO interface. The form of the element specific hysteresis loops MnO_2—SrO exhibits a nonconventional shape.

In the present work, we provide a theoretical explanation of these experimentally observed layer-specific element specific hysteresis loops. We combine model analysis with micromagnetic

simulations based on the input from first-principles density functional calculations. We show that the origin of the observed hysteresis loop is the bifurcation and the degeneracy that occur in the ground state magnetization of the system.

The different coercive fields for SRO and LSMO lead to a canted spin-configuration close to the LSMO-SRO interface, which is analyzed in detail. The complex interplay of interfacial antiferromagnetic exchange, anisotropy mismatch, and coercivity allows performing selective switching of SRO and LSMO layers.

In the spirit of a multiscale approach, we combined micromagnetic simulations for predicting a macroscopic, thermodynamic behavior with results from first principles calculations based on the density functional theory (DFT) within a generalized gradient approximation.[19] Structural parameters for the LSMO/SRO interface were taken from the previous first-principles studies.[20] However, we found that atomic relaxations at the interface have very little impact on electronic and magnetic properties, especially on the results of micromagnetic simulations. Using a self-consistent Green's function method under the paradigm of multiple scattering theory,[21,22] we utilized the magnetic force theorem[23] and estimated the exchange interaction strength between Mn and Ru moments at the LSMO/SRO interface. Hence, the approach presented here captures both microscopic quantum effects and emergent macroscopic statistical phenomena. It should be mentioned that both LSMO and SRO films are ferromagnetic.[24] The density of states (DOS) of the LSMO films is dominated by the contributions of the localized $3d$ states in both spin channels, separated by an exchange splitting order of 3.5 eV (see Fig. 1). In the SRO film, the superexchange interaction competes with the strong band magnetism of the Stoner type due to the substantial DOS at the Fermi level consisting mainly of $4d$ and $2p$ states of Ru and O atoms, respectively.[25] The coupling between LSMO and SRO films is strongly antiferromagnetic. The reason for the antiferromagnetic coupling is the indirect exchange interaction between the Mn and Ru magnetic moments via the interfacial oxygen atoms.[18,26,27]

The interface energy density of the LSMO-SRO system can be expressed as

$$E = -B\mu_1 \cos(\varphi_1 - \varphi_B) - B\mu_2 \cos(\varphi_2 - \varphi_B) - J\cos(\varphi_1 - \varphi_2) + \frac{K_1}{4}\sin^2(2(\varphi_1 - \varphi_{k_1})) + \frac{K_2}{4}\sin^2(2(\varphi_2 - \varphi_{k_2})), \quad (1)$$

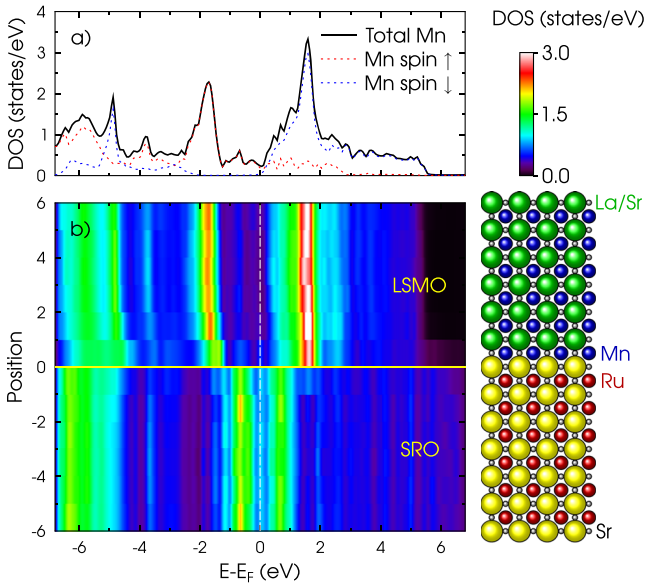

FIG. 1. Spin-resolved density of states (DOS) of Mn (a) and layer-resolved total DOS of the interface between LSMO and SRO films, as schematically depicted (b).

where B and φ_B are the amplitude and the orientation angle of the external magnetic field applied in the SRO and LSMO plane. φ_1, φ_2 define the in-plane orientation of the SRO and LSMO magnetizations μ_1, μ_2, respectively. The term $J\cos(\varphi_1 - \varphi_2)$ describes the antiferromagnetic coupling between the layers, and $\frac{K_i}{4}\sin^2(2(\varphi_i - \varphi_{k_i}))$ are the cubic magnetocrystalline anisotropy terms (with the energy density $K_{1,2}$). The exchange parameters $J_1 = -4.5$ meV and $J_2 = -13.3$ meV, entering Eq. (1) and corresponding to the interlayer antiferromagnetic interaction for two different interface terminations, were delivered by our first-principles calculations, as well as the magnetic moments of single Ru and Mn atoms ($\mu_1 = \mu_{\mathrm{Ru}} = 1.2\mu_B$, $\mu_2 = \mu_{\mathrm{Mn}} = 3.3\mu_B$). Typically for SRO/LSMO heterostructures, the magnetocrystalline anisotropy of the LSMO layer is negligible.[28] Hence, the influence of $K = K_1 = K_{\mathrm{SRO}}$ is decisive. For simplicity, we used dimensionless units, by expressing E in terms of the exchange $|J|$, rewriting the magnetic moments by $\mu_1 = \mu$, $\mu_2 = \beta\mu_1$, and introducing the parameter of interest $\alpha = K/|J|$. This also provides a rescaling of the magnetic field to $\tilde{B} = B\mu/|J|$. The dimensionless Hamiltonian

$$E/|J| = -\tilde{B}\left[\cos(\varphi_1 - \varphi_B) + \beta\cos(\varphi_2 - \varphi_B)\right] + \cos(\varphi_1 - \varphi_2) + \alpha\left[\frac{1}{4}\sin^2(2(\varphi_1 - \varphi_{k1}))\right] \qquad (2)$$

mainly depends on the model parameter α, whereas we compute the ratio β from DFT-based magnetic momenta giving $\beta = 2.75$, which corresponds to a system of equally thick layers of LSMO and SRO. Different thickness ratios can be described by manipulating this parameter. The positive sign of $+\cos(\varphi_1 - \varphi_2)$ is due to the antiferromagnetic exchange ($J/|J| = -1$). We explore the ground-state magnetic configuration through a minimization of the two-spin energy model functional Eq. (2) by means of the Monte Carlo method.

In the absence of the magnetocrystalline anisotropy term, the ground state minima are not separated by an energy barrier. Therefore, in the vicinity of zero field $\tilde{B} = 0$, small changes in the field result in jumps between minima, meaning a tiny coercive field. Figure 2(a) shows element specific hysteresis loops in the case of a zero magnetocrystalline anisotropy $\alpha = 0$. A strong magnetic field suppresses the antiferromagnetic exchange between the layers and aligns the magnetic moments along the external field. With a steady decline of the magnetic field, the impact of the antiferromagnetic exchange between layers becomes apparent. At certain critical values of the field, the ordering in the system changes. Since the magnetic moments of Ru and Mn atoms are different (the Ru moment is smaller), the Zeeman energy contributions are also different. Hence, the Ru moment flips by an angle of π, whereas the Mn retains its orientation at a finite bias field. The situation is different for the Mn moment. Instead of switching, the element specific hysteresis loop of the Mn atom exhibits a small valley that hints at a large Zeeman barrier compared with the characteristic energy scale of the antiferromagnetic inter-layer exchange. The magnetic moment of the Mn atom does not flip until the sign of the bias magnetic field changes.

Turning to the more realistic case of a finite magnetocrystalline anisotropy in the SRO layer [Fig. 2(b)], we note that the magnetocrystalline anisotropy of LSMO is relatively small and LSMO acts as a soft magnet. The significant difference in the strengths of the magnetic anisotropy imposes an asymmetry on the element specific hysteresis loops as it was experimentally demonstrated.[29] To a certain extent, the magnetocrystalline anisotropy can be controlled by strain, for instance, as induced by epitaxial growth on substrates of varying lattice constants.

By tuning the anisotropy of the SRO, we determine the critical bifurcation value, for which the hysteresis loops change abruptly [Fig. 2(b)]. This anisotropy prevents the SRO layer from flipping, whereas the LSMO has no anisotropy barrier and therefore switches first (blue solid line). At an elevated value of the magnetocrystalline anisotropy, the concave sector of the hysteresis loop smoothly disappears, meaning that the interlayer antiferromagnetic exchange has a negligible contribution to the formation of the hysteresis loop. The loop of the SRO layer is solely determined by the strong magnetocrystalline anisotropy and the large coercive magnetic field in this case. We call the critical strength of the anisotropy, for which the concave fragment of the hysteresis loop disappears, as the "bifurcation value."

The impact of the magnetic field direction with respect to the magnetocrystalline anisotropy axis is also of interest. Let us fix the magnetocrystalline anisotropy of the SRO at its critical bifurcation strength ($\alpha = 1$ for $\Delta\varphi = \varphi_B - \varphi_{k_1} = 0.25\pi$) and vary the relative angle $\Delta\varphi$, where φ_B defines the

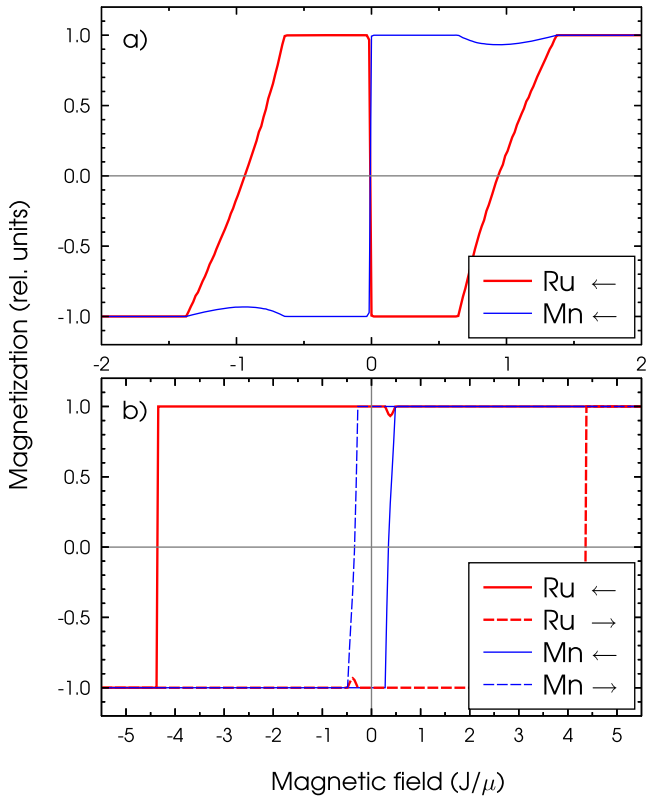

FIG. 2. Element specific hysteresis loops of Ru and Mn atoms for different ratios between the magnetocrystalline anisotropy of the SRO layer and antiferromagnetic exchange between layers: (a) $\alpha = K_1/|J| = 0$ and (b) $\alpha = K_1/|J| = 1.75$. The solid and dashed lines correspond to the different directions of steering of the applied magnetic field (from positive $\tilde{B}$ to negative and vice versa, as indicated by arrows). Parameters: $\varphi_B = \varphi_{k_1}, \beta = \mu_{\mathrm{Mn}}/\mu_{\mathrm{Ru}} = 2.75$ for the magnetic moments of single Ru and Mn atoms, respectively. The transition at the critical ratio meaning the critical strength of the anisotropy for which the concave fragment of the hysteresis loop disappears is equal to $\alpha = K_1/|J| = 1.75$ (b) in the case of $\varphi_B = \varphi_{k_1}$.

orientation of the magnetic field and φ_{k_1} corresponds to the easy axis of the anisotropy of the SRO layer. The results of numerical calculations are shown in Fig. 3. As it is evident from Fig. 2(a), as long as the external field is applied parallel to the easy axis and the relative angle is small $\Delta\varphi = 0$, the concave sector of the SRO hysteresis loop is small, meaning the anisotropy barrier to be too high and the coercive field to be too strong. With an increase in the non-collinearity between the external field and the anisotropy axis, the concave sector of the hysteresis loop becomes larger and acquires the shape different from conventional rectangular hysteresis loops. The strongest effect we observed is for $\Delta\varphi = 0.25\pi$. The coercive fields for SRO and LSMO are different, which allows performing a selective switching (Fig. 3).

The critical regime $\alpha \approx 1$ for $\Delta\varphi = 0.25\pi$ [Fig. 3(a)] is rather sensitive to slight changes in $\Delta\varphi$. Beyond the critical regime, the concave sector disappears [Fig. 3(c)], leading to reordering of the switching (SRO layer switches first).

A further insight is gained from the energy landscape in Fig. 3(b). The dots A and B on the hysteresis loop [Fig. 3(a)] are marked on the energy landscape [Fig. 3(b)] by white dots on the left A and right B figures, respectively. The local minima are separated by an anisotropy barrier [Fig. 3(b)]. Therefore, for point A, the switching is prohibited, while for point B the switching is permitted. The critical strength of the magnetocrystalline anisotropy K [Fig. 1(b)] depends also on the direction of the magnetic field $\Delta\varphi$. The role of a thermal activation follows from finite temperature magnetic dynamics simulations, as detailed next.

Not only the influence of a finite temperature on the magnetization dynamics but also the finite layer thickness, potentially leading to a non-collinear magnetic configuration within the LSMO or

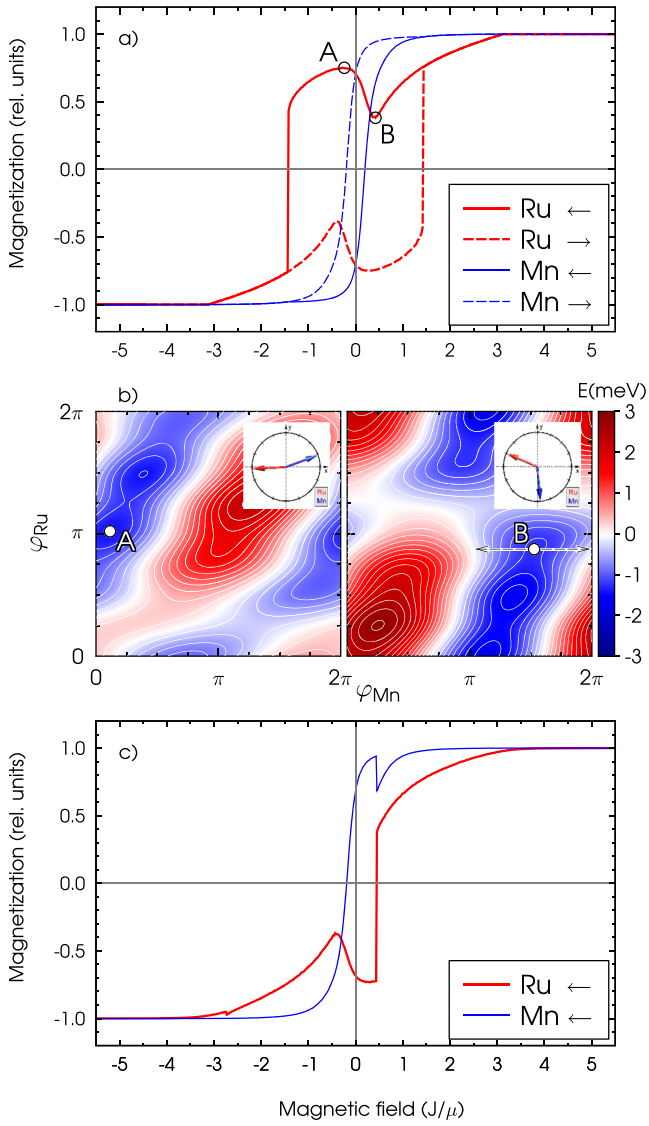

FIG. 3. Element specific hysteresis loops of Ru and Mn atoms for different offsets between the external field's angle φ_B and the anisotropy's easy axis direction φ_{k_1} in the vicinity of the critical difference: (a) $\Delta\varphi = 0.25\pi$ and (c) $\Delta\varphi = 0.26\pi$. The solid and dashed lines correspond to the different directions of steering of the applied magnetic field (from positive $\tilde{B}$ to negative and vice versa, as indicated by arrows). (b) shows energy-surfaces for the labeled points (A, B) in (a). The horizontal arrow around point B illustrates the flexibility of switching of the Mn-moment, i.e., the range where the angle φ_{Mn} can be steered in the interval $\pi < \varphi_{Mn} < 2\pi$ without altering the angle φ_{Ru}. The inset illustrates the spin-configuration at these fields. Parameters: $\alpha = 1$; $K_2 = 0, \beta = 2.75$.

SRO components, is considered in our micromagnetic simulations. On top of that, the two different interface terminations are considered explicitly, leading to different strengths of the antiferromagnetic interlayer exchange. Following Ref. 28, we adopt atomistic parameters for micromagnetic calculations. The exchange stiffness reads $A \approx \frac{JS^2 Z_c}{a_0}$ with Z_c being the number of magnetic atoms per unit cell, J being the classical Heisenberg exchange constant, and S being the magnetic moment of a single magnetic atom. In our case, the exchange parameter already includes the absolute value of the magnetic moments. The considered crystal structures contain only one magnetic atom per unit cell and hence $A \approx J/a_0$ holds. For the particular value $a_0 = 4$ Å, the resulting exchange stiffness is shown in Table I. The values for the exchange constant J and the magnetic moment μ follow from our density functional theory calculations.

TABLE I. Comparison of atomistic and micromagnetic parameters.

	J (meV)	μ (μ_B)	A (pJ/m)	Thickness (uc)
SRO	4.5	1.2	1.80	16
LSMO	13.3	3.3	5.46	9

TABLE II. Saturation magnetization and cubic magnetocrystalline anisotropy constant (Ref. 28).

	M_{sat} (MA/m)	K_{c1} (kJ/m^3)
SRO	0.20	640
LSMO	0.56	−2

The experimental data concerning the magnetocrystalline anisotropy and the saturation magnetization are presented in Table II. The free energy density of the system can be cast as

$$F = F_{\text{EX}} + F_{\text{Z}} + F_{\text{DMF}} + F_{\text{MCA}}. \tag{3}$$

Here F_{EX} corresponds to the exchange interaction, F_{Z} is the Zeeman energy for the applied static magnetic field, F_{DMF} describes the contribution of the demagnetizing field that arises due to the finite size of the system, and F_{MCA} is the magnetocrystalline anisotropy term. All parameters entering the free energy density are delivered by our DFT results or experiment. For the interlayer antiferromagnetic exchange coupling term, we consider the interaction only between the nearest neighbor atoms at the interface. For two surface terminations, we have two different interfacial exchange constants $J_{1,2} = -J_1$, $J_{1,2} = -J_2$ correlating to two different interfacial exchange stiffness constants A.

The magnetization dynamics is governed by the stochastic, finite temperature Landau-Lifshitz-Gilbert (LLG) equation

$$\dot{\mathbf{m}}(t) = -\frac{\gamma}{1+\alpha^2}\left[\mathbf{m}\times\mathbf{H}^{\text{eff}} + \alpha\mathbf{m}\times\left(\mathbf{m}\times\mathbf{H}^{\text{eff}}\right)\right]. \tag{4}$$

Here $\gamma = \gamma_0\mu_0$, with the gyromagnetic constant $\gamma_0 = 1.76\times10^{11}1/(\text{Ts})$, the vacuum permeability $\mu_0 = 4\pi\times10^{-7}$ Tm/A and the Gilbert damping α. The effective magnetic field in Eq. (4) consists of two contributions: the functional derivative of the free energy density and the stochastic thermal random magnetic field due to thermal (white) noise,

$$\vec{H}^{\text{eff}}(t) = -\frac{1}{\mu_0 M_s}\frac{\delta F[\vec{m}]}{\delta\vec{m}} + \vec{h}(\vec{r},t). \tag{5}$$

The noise correlation function is

$$\left\langle h_{ik}(t)h_{jl}(t+\triangle t)\right\rangle = \frac{2k_BT\alpha}{\gamma M_s a_0^3}. \tag{6}$$

i and j define the corresponding sites on the surface, k and l correspond to the Cartesian components of the random magnetic field, and T is the temperature.

Micromagnetic simulations are performed using the graphics processing unit (GPU) accelerated code package mumax3,[30] which enables us to consider the influence of demagnetizing fields efficiently. The sample is discretized in cubic cells with a size of $(1.2\text{ nm})^3$ and a grid of $50\times50\times8$ cells, where SRO occupies five layers and LSMO occupies three layers as an approximation for the actual experimental system size. In the x and y directions, periodic boundary conditions are assumed as the lateral dimension of the sample is much larger than its thickness. A classical fourth-order Runge-Kutta method is chosen to solve the differential equation with a fixed time step of $\delta t = 0.05$ ps.

Several hysteresis loops are shown in Fig. 4 depending on the surface termination and the temperature. The general trend is similar to the two-spin approach presented before. The main results of the micromagnetic simulations are the unequal shapes of hysteresis loops for different

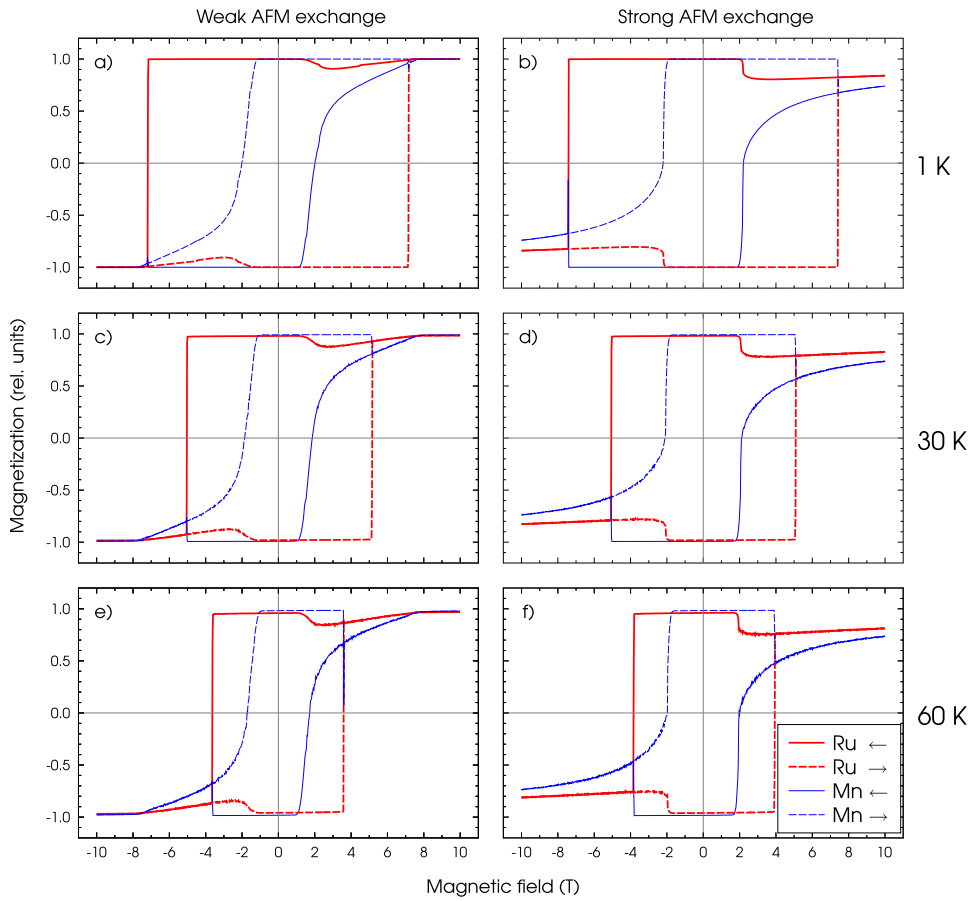

FIG. 4. Hysteresis loops determined from micromagnetic simulations for different interface terminations involving weak (left panel) and strong (right column) antiferromagnetic interlayer exchange. The temperature is increased in every row, from 1 K [(a) and (b)] over 30 K [(c) and (d)] up to 60 K [(e) and (f)]. External field and anisotropy axes are oriented parallel. The system is discretized in $50 \times 50 \times 8$ unit cells [$V = (1.2\ \text{nm})^3$] with periodic boundary conditions in the lateral directions.

interlayer exchange constants and the diminished energy barrier at elevated temperatures. For a stronger exchange coupling, both layers switch in a rather steep manner compared to the case of a weak coupling [cf. Figs. 4(b), 4(d), and 4(f)].

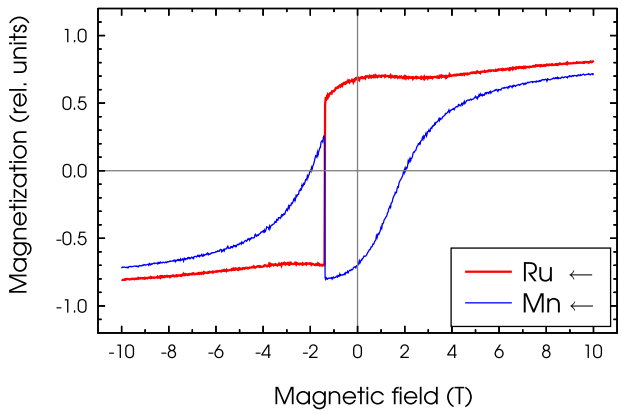

FIG. 5. Hysteresis loop obtained from micromagnetic simulations for $T = 60$ K and $\Delta\varphi = \pi/4$. The system is discretized in $50 \times 50 \times 8$ unit cells [$V = (1.2\ \text{nm})^3$] with periodic boundary conditions in the lateral directions.

A similar behavior is observed in the case of non-collinear external and magnetocrystalline fields. Hysteresis curves are smooth; concave patterns are not observed (see Fig. 5 for $T = 60$ K and $\Delta\varphi = \pi/4$). Comparing the micromagnetic results for an extended system with the Monte Carlo model approach, we note that, for a heterostructure with a finite thickness, the magnetization relative alignment is averaged over each layer. Besides, the effect of the inter-layer exchange interaction in our calculation was considered only for nearest neighbor magnetic moments. Therefore, the concave sector-pattern is less pronounced for the extended system. Nevertheless, a canting of the magnetic moments is evident and can be extracted from the data, which can be seen in Fig. 6. The arrows represent the magnetization's average orientation for each layer of the system's discretization. Due to the weak anisotropy in the LSMO, the non-collinear texture can mainly be seen in the Mn-component of the magnetic moments, but also the SRO is affected close to the interface.

Interfacing the ferromagnetic oxides $La_{0.7}Sr_{0.3}MnO_3$ (LSMO) and $SrRuO_3$ (SRO) results in an interfacial antiferromagnetic exchange coupling. In the spirit of the exchange bias, we expect to find an element specific modification of the hysteresis loops of LSMO/SRO stacks. Using a combination of first-principles calculations and finite-temperature micromagnetic simulations, we uncover the origin of the shape of hysteresis loops and their dependencies on external parameters. The findings point to a general phenomenon resulting from an interplay of magnetization, coercivity, and anisotropy contributions at the interface of two ferromagnetic oxide materials with the result mimicking what is seen in exchange-bias systems. It could be as useful as common exchange-bias systems but further allows for a selective switching of the individual layers. Subsequent studies are planned in two main directions. Obviously the thickness of the magnetic layers will directly influence the impact on the AFM interlayer exchange on the switching characteristics. Special focus should be put on depth-dependent spin-canting and selective switching processes, as shown in the macrospin approach. On the other hand, the impact of modifications of the anisotropy due to the oxide interface is worth studying as it will directly influence the canted spins' structure and position relative to the interface. Ultimately controlling non-collinear spin structures enables also the control of electronic transport

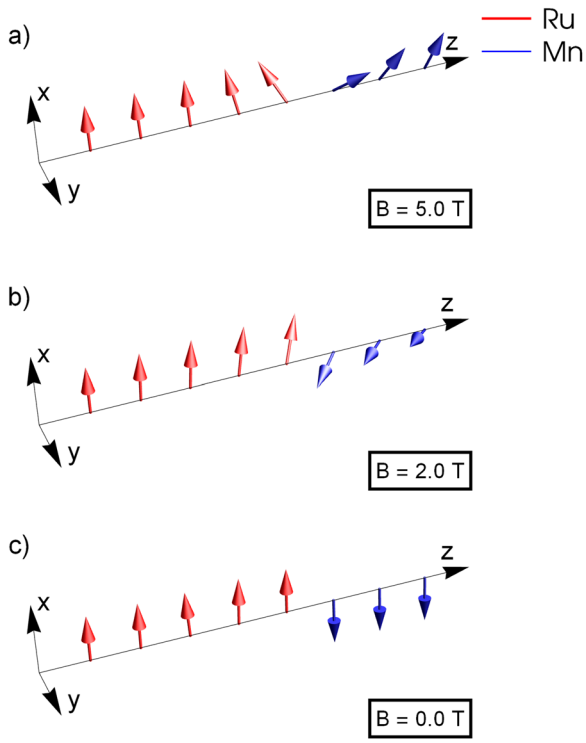

FIG. 6. Spin configurations for three different magnetic field strengths pointing in the x-direction, corresponding to [Fig. 4(a)]. The arrows represent average magnetic orientation in a layer of the simulation's discretization lattice.

properties as the electron spin polarization is directly manipulated. This ability is highly desirable for applications in spintronic devices.

This work is supported by the DFG within the Collaborative Research Center SFB 762, "Functionality of Oxide Interfaces."

[1] W. H. Meiklejohn and C. P. Bean, Phys. Rev. **102**, 1413 (1956).
[2] J. Nogues and I. K. Schuller, J. Magn. Magn. Mater. **192**, 203 (1999).
[3] J. Camarero, J. Sort, A. Hoffmann, J. M. Garcia-Martin, B. Dieny, R. Miranda, and J. Nogues, Phys. Rev. Lett. **95**, 057204 (2005).
[4] J. Nogues, J. Sort, V. Langlais, V. Skumryev, S. Surinach, J. S. Munoz, and M. D. Baro, Phys. Rep. **422**, 65 (2005).
[5] Y. Bai, G. Yun, and N. Bai, J. Appl. Physics **107**, 033905 (2010).
[6] R. L. Stamps, J. Phys. D: Appl. Phys. **33**, R247 (2000).
[7] P. Miltenyi, M. Gierlings, J. Keller, B. Beschoten, G. Güntherodt, U. Nowak, and K. D. Usadel, Phys. Rev. Lett. **84**, 4224 (2000).
[8] A. Scholl, M. Liberati, E. Arenholz, H. Ohldag, and J. Stöhr, Phys. Rev. Lett. **92**, 247201 (2004).
[9] M. R. Freeman, A. Y. Elezzabi, and J. A. H. Stotz, J. Appl. Phys. **81**, 4516 (1997).
[10] P. Borisov, A. Hochstrat, X. Chen, W. Kleemann, and C. Binek, Phys. Rev. Lett. **94**, 117203 (2005).
[11] J. C. Mallinson, *Magneto-Resistive and Spin Valve Heads: Fundamentals and Applications* (Academic Press, 2001).
[12] X. Ke, M. S. Rzchowski, L. J. Belenky, and C. B. Eom, Appl. Phys. Lett. **84**, 5458 (2004); J. Appl. Phys. **97**, 10K115 (2005).
[13] W. Eerenstein, N. D. Mathur, and J. F. Scott, Nature **442**, 759 (2006).
[14] N. A. Spaldin and M. Fiebig, Science **309**, 391 (2005).
[15] S. W. Cheong and M. Mostovoy, Nat. Mater. **6**, 13 (2007).
[16] S. Park, Y. J. Choi, C. L. Zhang, and S. W. Cheong, Phys. Rev. Lett. **98**, 057601 (2007).
[17] R. N. Rogers, L. Finegold, and B. Morosin, Phys. Rev. B **6**(3), 1058 (1972).
[18] S. Das, A. D. Rata, I. V. Maznichenko, S. Agrestini, E. Pippel, K. Chen, S. M. Valvidares, H. Babu Vasili, J. Herrero-Martin, E. Pellegrin, K. Nenkov, A. Herklotz, A. Ernst, I. Mertig, Z. Hu, and K. Dörr, e-print arXiv:1606.08687.
[19] J. P. Perdew, K. Burke, and M. Ernzerhof, Phys. Rev. Lett. **77**, 3865 (1996).
[20] K. Lv, H. P. Zhu, W. Q. Zou, F. M. Zhang, and X. S. Wu, J. Appl. Phys. **117**, 185305 (2015).
[21] M. Lüders, A. Ernst, W. M. Temmerman, Z. Szotek, and P. J. Durham, J. Phys.: Condens. Matter **13**, 8587 (2001).
[22] M. Geilhufe, S. Achilles, M. A. Köbis, M. Arnold, I. Mertig, W. Hergert, and A. Ernst, J. Phys.: Condens. Matter **27**, 435202 (2015).
[23] A. I. Liechtenstein, M. I. Katsnelson, V. P. Antropov, and V. A. Gubanov, J. Magn. Magn. Mater. **67**, 65 (1987).
[24] C. Zener, Phys. Rev. **82**, 403 (1951).
[25] C. Etz, I. V. Maznichenko, D Böttcher, J. Henk, A. N. Yaresko, W. Hergert, I. I. Mazin, I. Mertig, and A. Ernst, Phys. Rev. B **86**, 064441 (2012).
[26] Y. Lee, B. Caes, and B. Harmon, J. Alloys Compd. **450**, 1 (2008).
[27] M. Ziese, I. Vrejoiu, E. Pippel, P. Esquinazi, D. Hesse, C. Etz, J. Henk, A. Ernst, I. V. Maznichenko, W. Hergert, and I. Mertig, Phys. Rev. Lett. **104**, 167203 (2010).
[28] J. M. D. Coey, *Magnetism and Magnetic Materials* (Cambridge University Press, 2009).
[29] C. Du, R. Adur, H. Wang, A. J. Hauser, F. Yang, and P. C. Hammel, Phys. Rev. Lett. **110**, 147204 (2013).
[30] A. Vansteenkiste, J. Leliaert, M. Dvornik, M. Helsen, F. Garcia-Sanchez, and B. Van Waeyenberge, AIP Adv. **4**(10), 107133 (2014).